Optimal Bending Stiffness Design of a Soft Micro-Robot for Cochlear Implantation

Alexandre Thuillier, Sébastien Krut, Nabil Zemiti, Philippe Poignet

Optimal Bending Stiffness Design of a Soft Micro-Robot for Cochlear Implantation

Alexandre Thuillier, Sebastien Krut, Nabil Zemiti, Philippe Poignet

Abstract— In this paper, a design method for a Soft Micro-Robot (SMR) used for medical intervention in the context of cochlear implant insertion is proposed. Optimal design of cochlear implants has been a highly active research area in recent years. Dozens of articles address the topic of optimal design using different actuation strategies, resulting overall in promising outcomes. From magnetic to fluid actuation and concentric tubes, current strategies are based on generating an optimal bending moment. However, this approach gives optimal results that cannot be manufactured. Considering the manufacturing constraints of micro-scale soft robots, an optimal design method based on varying the robot bending stiffness is studied here. The cochlear implant is actuated by a tendon and has an optimal bending stiffness to achieve a given objective. In the context of cochlear insertion, this objective is to minimize the root mean square error (RMSE) of the robot neutral axis in comparison to the cochlea helicoidally shaped centerline. Simulation results are promising with an average distance error of 392 μm and a standard-deviation of 33 μm considering the robot material and manufacturing uncertainties.

I. INTRODUCTION

Hearing impairment affects millions of people worldwide and over 40 million in the U.S. only. Adults encountering hearing loss is idiopathic or noise induced. Potential solutions involve hearing aids, corticosteroids, or cochlear implants [1], the latter being the focus of this study.

Cochlear Implants (CI) by-pass the natural auditory mechanism, converting sound waves into an electrical stimuli by directly stimulating the auditory nerve within the inner ear as illustrated in Fig. 1. CI works with a microphone capturing acoustic waves which is connected to a speech processor and a transmitter placed behind the ear. This speech processor converts acoustic waves into electric signals that are then sent to a receiver positioned within the mastoid bone behind the external ear. The generated electric signal travels along wires down to the inner ear in which the auditory nerve is electro-stimulated by electrodes and interpreted as sound by the brain.

To achieve this implantation, an access to the middle-ear must be done with a surgical procedure by opening the mastoid [2] and drilling into the temporal bone depicted in Fig. 1. Once into the middle-ear, surgeons have a direct sight of the cochlea entrance. This snail-shaped-like bone is made of three helicoidally shaped canals including the Scala Tympani (ST) inside which the cochlear implant (Fig. 1) is inserted thanks to a forceps held by the surgeon's hand.

However, while the cochlea entrance is at sight, the surgeon cannot see inside the cochlea which pushes the surgeon to rely only on force feedback during the cochlear implantation into the ST. The cochlea inner anatomy having
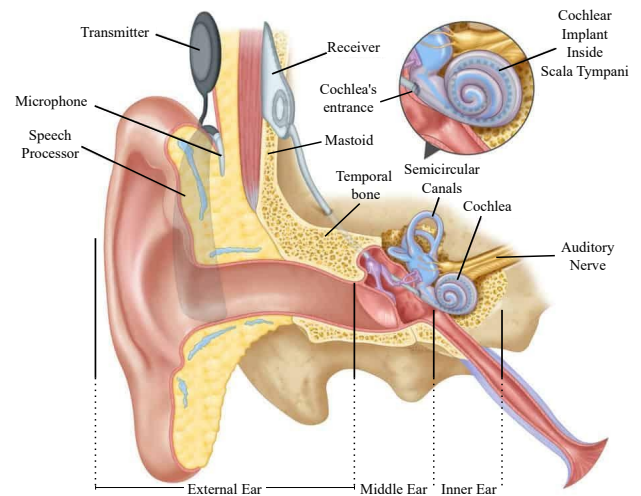

Fig. 1. A cochlear implant within the cochlea [4]

a breaking threshold close to what the surgeon can perceive with her/his hand put a risk of intra-cochlear trauma [3] and may potentially lead to total deafness for patients with a low residual hearing. Due to these risks, the procedure is typically performed for individuals with very low residual hearing or total deafness which is an issue as preserving residual hearing helps for future recovery.

Commercially available solutions exist, comprising two distinct CI types: the straight CI with an optimally shaped distal tip for low contact forces against the anatomic walls and the pre-curved perimodiolar electrode array which is able to be inserted with as little contacts as possible. But, the aforementioned solutions are not optimal as the straight CI still relies on the interaction with the anatomy to slide into the ST and the perimodiolar CI may buckle during the insertion which must be removed afterward with a lot of trauma on the inner ear. Both implants types use flexible materials and are very slender. Their embedded electrodes and wires, composed of alloys, contribute to their structural integrity.

A. Related Work

While interesting, these commercial solutions are not optimal like an active control of the cochlear implant during the insertion could be. This should permit to follow the helicoidally shaped ST, keeping distance of the anatomic wall without buckling.

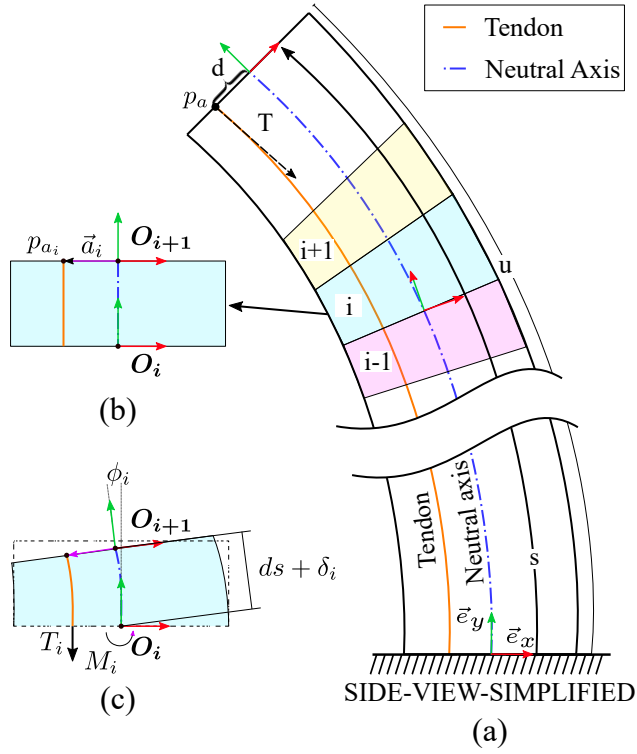This concept of active implant with an intrinsic actuation

Fig. 2. (a) FEM scheme of a tendon actuated cantilever beam (b) a beam element i at rest (c) a beam element i under load

transforms the cochlea implant into a soft micro-robot which is studied wildly as in [5], [6] with a magnetic force/torque control of the CI distal tip or concentric tubes [7], fluidic [8], [9] and finally with an actuation tendon [10] which is inspired by steerable continuum robots.

In this paper, the reader is expected to see a methodology to design a soft and slender micro-robot to achieve active shape objective. The focus is on the optimal design of an intrinsically actuated straight lateral wall cochlear implant by the means of an actuation tendon. As stated in [10], the choice of a tendon is motivated by the limited space available in the cross-section. Also, no embedded permanent magnet may interfere with external magnetic fields and no heavy material solicitation of the highly pressurized fluidic actuator is happening as in the fluidic actuators. This paper differs from the work of [10] as their strategy of finding the optimal tendon position for an optimal bending moment is constrained by the fabrication process. Here, finding the optimal bending stiffness with a constant tendon positioning is studied and shall be accurately manufacturable by soft lithography [11].

II. Analytical Modeling Approach

A. Statics

First, an elastic model of a steerable cochlear implant from [10] is used to compute the forward kinematic. The cochlear implant is virtually discretized in N sub-elements of length $ds = u/N$ with N the number of elements and u

the total length of the robot as illustrated in Fig. 2 (a). To proceed so, the cochlear implant is considered as a cantilever beam discretized in beam elements loaded by an actuation tendon. This tendon is running along its own longitudinal axis oriented by the local $\vec{e}_y$ and anchored at the robot tip p_a as illustrated in Fig. 2. The tendon anchor point p_a position is offset with respect to the beam neutral axis and acts as a lever arm at a distance $d = ||\vec{a}||$ defined in section II-B. Therefore, when the tendon is subjected to a tension T, a reacting bending moment M around $\vec{e}_z$ is acting on the beam-element support:

$$\vec{M} = \vec{a} \times \vec{T} \qquad (1)$$

then, with the assumptions that:

- Material is linearly elastic in axial and bending deformations
- Material is homogeneous over the beam length
- Cross-section over a small beam element remains planar with minimal deformation

The deflection of a beam element can be modeled as expressed in Eq. 3 taking into consideration the shrinkage δ along its longitudinal axis $\vec{e}_y$ and the deflection ϕ around the normal vector $\vec{e}_z$. Both deformations are respectively dependent on the axial and bending stiffness of the beam noted K_a and K_b which are defined from the robot material and geometric properties:

$$K_b = \frac{EI_{zz}}{ds}, \quad K_a = \frac{EA}{ds} \qquad (2)$$

with the Young's modulus E, the second moment of area I_{zz}, the cross-section area A and length ds of the beam elements:

$$\begin{bmatrix} \delta \\ \phi \end{bmatrix} = \begin{bmatrix} K_a^{-1} & 0 \\ 0 & K_b^{-1} \end{bmatrix} \begin{bmatrix} \vec{e}_y^T & \vec{0} \\ \vec{0} & \vec{e}_z^T \end{bmatrix} \begin{bmatrix} \vec{T} \\ \vec{M} \end{bmatrix} \qquad (3)$$

It is now possible to compute Eq. 3 for each sub-segments i along the robot neutral axis and retrieve the position of the top surface center of any subsegment i iteratively:

$$\mathbf{O}_{i+1} = \vec{c}_i + \mathbf{D}_i((ds + \delta_i)\vec{e}_{yi} - \vec{c}_i) \qquad (4)$$

with $\mathbf{D}_i = e^{\vec{e}_{zi}\phi_i}$, $\vec{e}_{zi}$ the bending axis and $\vec{c}_i$ the Center of Gravity (CoG) calculated in Sec. II-B represented as $\mathbf{O}_i$ in Fig. 2. Iteratively :

$$^0\mathbf{R}_i = \prod_{k=0}^{i-1} {}^k\mathbf{R}_{k+1} \text{ where } {}^{i-1}\mathbf{R}_i = \mathbf{D}_i \qquad (5)$$

$$\mathbf{O}_i = \sum_{k=0}^{i-1} \mathbf{R}_k \mathbf{O}_{k+1} \text{ where } \mathbf{O}_1 = \vec{0} \qquad (6)$$

B. Varying bending stiffness

The bending stiffness K_b given by Eq. 2 is now considered non-constant over the robot length noted $s \in [0, u]$ depicted in Fig. 2 (a):

$$K_b(s) = \frac{EI_{zz}(s)}{ds} \qquad (7)$$

The robot cross-section has been modified with two new canals expanding from the robot base at $s = 0$ to its distal tip at $s = u$ and parallel to the original tendon canal as illustrated in Fig. 4 (a, b, c). In a small beam element, the number of holes in its cross-section has now been count to three: left, center and right hole. The actuation tendon will fit within the center hole and its dimensions will remain constant along the robot length s while the two others adjacent symmetric holes will vary along s.

The total second moment of area of a small beam element cross-section i is calculated as a sum of all the sub cross-sections that may be holes or filled using the parallel axis theorem:

$$I_{zz}(s) = \sum_{j=0}^{J} \lambda_j (I_j(s) + A_j(s) r_j^2(s)) \tag{8}$$

with $j = [0, 1, 2]$ respectively: left, center and right hole, λ equals to -1 for a hole and 1 for material, I_j the second moment of area of the sub cross-section wrt its own centroid c_j, A_j the area of the j-th cross-section and $r_j = ||\vec{c}_i - \vec{c}_j||$ the distance of the j-th sub cross-section CoG to the i-th beam element CoG. These rectangles second moment of area are constrained by the manufacturing process as it is quite challenging to create a variable height at this scale. Therefore, for each $I_j(s)$, only the sub cross-section width b_j is considered variable while its height $h_j = h_1$ remain constant along the whole robot length s:

$$I_j(s) = \frac{b_j(s) h_1^3}{12} \tag{9}$$

By changing the cross-section geometry, the bending stiffness K_b is not the only parameters affected in the beam element. Indeed, the cross-section area A and the CoG, by which the neutral axis passes through, depend on this geometry. This changes the lever arm d for each beam-element i that is defined as the distance between the tendon anchor point p_{a_i} and the CoG c_i:

$$\vec{c}_i = \frac{\vec{o} A - \sum_{j=0}^{J} \vec{r}_j A_j}{A - \sum_{j=0}^{J} A_j} \tag{10}$$

with $j = [0, 1, 2]$ respectively: left, center and right hole, $\vec{o} = \vec{0}$ and $A_j = b_j h_1$. Therefore:

$$d_i = ||\vec{a}_i|| = ||\vec{p}_{a_i} - \vec{c}_i||^2 \tag{11}$$

The previously constant Eq. 3 for a beam element i can now be expressed as:

$$\begin{bmatrix} \delta \\ \phi \end{bmatrix} = \begin{bmatrix} K_a^{-1}(s) & 0 \\ 0 & K_b^{-1}(s) \end{bmatrix} \begin{bmatrix} \vec{e}_y^T & \vec{0} \\ \vec{0} & \vec{e}_z^T \end{bmatrix} \begin{bmatrix} \vec{T} \\ \vec{M}(s) \end{bmatrix} \tag{12}$$

which can be computed recursively from $i = 0$ to N to determine the robot distal tip position.
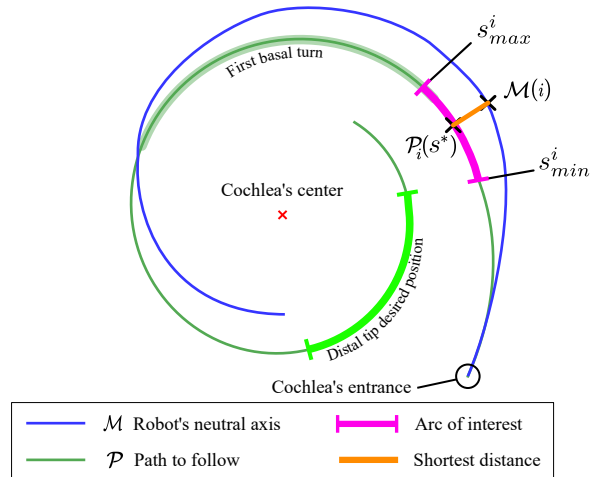

Fig. 3. Comparaison between the robot neutral axis and scala tympani centerline. The thick translucent green line on $\mathcal{P}$ represent the first turn in the scala tympani where high contact forces may happen during a cochlear implantation

III. METHODS AND MATERIALS

In the context of CI robotization, generating an optimal bending stiffness can be addressed in three ways: heterogeneous bulk materials, crave the outside material or hollow-out the inside materials. In this paper, we hollowed-out some material at specific point to reduce the stiffness of the robot along its longitudinal axis to achieve a non-circular bending shape. This design method can be easily manufactured by soft lithography but it imposes a constant height of the inner chambers along the robot longitudinal axis [11]. Coming along with the previous constrains, the cochlea anatomy and the current CI geometries are considered and are the same as our previous work in [12].

A. Design Objective

Lateral wall straight cochlear implants are known to use contacts against the anatomy to bend and crawl with a high magnitude of forces leading to traumas in the first turn of the ST as illustrated in Fig. 3. Therefore, the objective is to minimize the RMSE between the robot and ST centerlines as follows:

$$\min_{b_j^i, h_0, T} \Psi = \sqrt{\frac{\sum_{i=1}^{N} ||\mathcal{P}(s^*) - \mathcal{M}(i)||^2}{N}} \tag{13}$$

$$\text{subject to} : s^* = \underset{s \in [s_{min}, s_{max}]}{\arg \min} ||\mathcal{P}(s) - \mathcal{M}(i)||$$

with $s \in [0, u]$ the position on $\mathcal{P}$ and b_j^i, h_0, T respectively the optimal width of the adjacent symmetric holes with the symmetry constraint $b_0^{i*} = b_2^{i*}$ and the bottom membrane height, T is tendon tension, N the number of beam elements (Sec. II-A), $\mathcal{P}$ and $\mathcal{M}$ are the ST and robot centerlines, s^* the closest point on $\mathcal{P}$ between $\mathcal{M}(i)$ and the path $\mathcal{P}$. $[s_{min}, s_{max}]$ is an arc length on the path $\mathcal{P}$ where s^* must
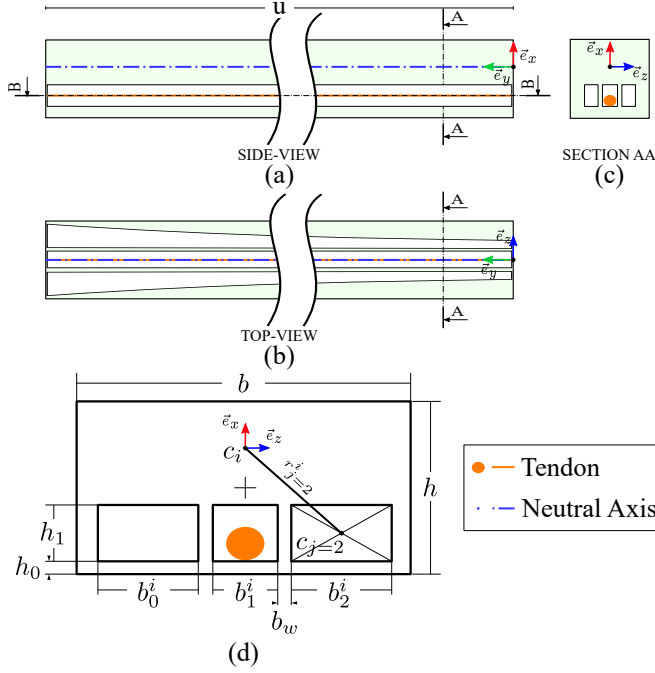
Fig. 4. (a) Side view of the actuated robot, (b) robot top view with the three adjacent holes and their varying width from the robot base to its tip, (c) the robot cross-section AA, (d) a zoomed schematic of the geometric parameters used in the bending stiffness optimization

be found, as depicted in Fig. 3. Initially $s_{min} = 0$ and $s_{max} = ds$, and for each step $i \in [0, N]$, $^{i+1}s_{min} = ^{i} s^*$ and $^{i+1}s_{max} = ^{i+1} s_{min} + ds$.

B. Design Constraints

1) Anatomical: The soft robot size shall be constrained by the ST geometry that varies greatly between individuals [13]. So only average values will be considered knowing that patient-specific active cochlea implant could be designed.

Insertion by the scala tympani entry point as illustrated in Fig. 1 is assumed. Once inside the ST, its dimensions are 2.1mm wide for 1.30mm high at its base and 1.31mm wide for 0.72mm high after roughly 1 turn where the CI distal tip desired position shall be for a device this long as illustrated in Fig. 3. The logarithmically spiral shaped path $\mathcal{P}$ to follow is generated by a phenomenological model of the scala tympani centerline [14]. Finally, as the helicoidally shaped ST has an elevation of only ∼1mm after the first basal turn, a 2D study is considered as a proof of feasibility. It shall be supported by a 3D study subsequently only if deeper insertion is needed but the CI electro-stimulation beyond the depth of 25 mm or 1 1/4 turn into the cochlea (Fig. 3) does not seem necessary [15], [13].

2) Geometrical Constraints: The current trend for newly developed CI is a length of around 20 mm to 25 mm for the best balance between cochlea trauma and performance. The smallest distal height is approximately 0.4 mm and the biggest 0.5 mm while the basal diameter ranges between 0.6 and 1.3 mm [15], [16].

Robot geometric parameters		Value	Units
Height	h	700	μm
Width	b	700	μm
Length	u	25	mm
Optimization parameters		**Interval**	**Units**
Membrane height	h_0	[100, 200]	μm
Chambers height	h_1	[d_t, 400]	μm
Chamber width	b_j^i	[0.0, 180]	μm
Tendon tension	T	[0.0, 100]	mN

Fig. 2 (b) depicts the device of a length $u = 25$ mm, height of $h = 0.7$ mm and a constant width of $b = 0.7$ mm. Since the length u and width b of this CI are based on a commercially available cochlear implant, it is important to fix those parameters as constants.

Finally, the optimal width $b_j^{i^*}$ depicted in Fig. 4 (d) for the right and left holes must satisfy a geometric constraint to consider the structural cohesion: the maximum holes width must be within the robot total width considering the inner wall thickness b_w between holes and the middle can for the actuation tendon. Similarly, h_0^* must be smaller than the robot total height h.

C. Analysis

1) Setup: A Python script has been written to integrate the finite element modeling described in Sec. II-A. The "bruteforce" method from the "scipy" library has been used to find a global minimum for Eq. 13. The optimization parameters h_0 and h_1 remain constant over the robot longitudinal axis for each i in $[0, N]$, the solution is found on a defined sparse grid as these parameters will be manufactured by a process called spin-coating [11] which may not be as accurate as a planar parameter as $b_j^{i^*}$. The optimization parameters h_0 and h_1 are found on a defined sparse grid as these parameters will be manufactured by spin-coating [11] which may not be as accurate like the planar parameter $b_j^{i^*}$. On the contrary, $b_j^{i^*}$ can be manufactured with micro-metric accuracy thanks to the manufacturing process [11] which gives us the opportunity to use a polishing function so an optimal solution is found on the grid of points to seek a more precise minimum for $b_j^{i^*}$.

2) Robot Material: As stated previously in Sec. II-A, linear elasticity is supposed with an averaged Young's modulus of E=2.12 MPa for the elastomer PDMS [17].

3) Workflow: Initially, the width $b_j^{i^*}$ is set to 0 mm for maximum bending stiffness, h_1 is equal to the tendon diameter to assure that it can fit inside its own canal and T is initially guessed with a minimization of Eq. 13 with the initial parameters aforementioned.

4) Verification: A sensitivity analysis is performed as uncertainties due to the material identification or the manufacturing process may lead to inaccuracy. Afterward, a
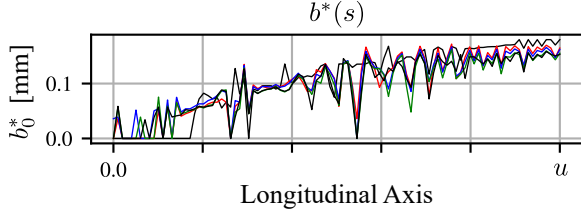
Fig. 5. Differents optimization results of the varying holes' width b_j^i along the robot longitudinal axis $s \in [0, u]$ at constant h_0^* and h_1^* over s

TABLE II

DESIGN OPTIMIZATION RESULTS

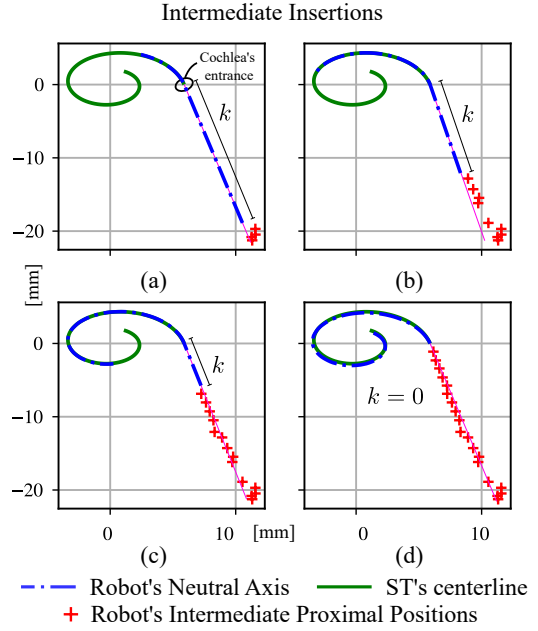| Optimization results		Value	Units
Membrane height	h_0^*	183.5	μm
Chambers height	h_1^*	400	μm
Chamber width	b_j^{i*}	[0.0, 158.4]	μm
Tendon tension	T^*	64.6	mN
Objective function	Ψ	391.77	μm

Fig. 6. Intermediate insertion results at (a) $k = 0.75N$ (b) $k = 0.5N$ (c) $k = 0.25N$ (d) $k = 0$, the red crosses represents the robot intermediate proximal positions. The thin magenta line behind the robot neutral axis is the sheath.

complete insertion with the optimal geometric parameter is simulated to search for an optimal orientation and proximal pose of the robot to guarantee an optimal complete insertion path with good alignment of $\mathcal{P}$ and $\mathcal{M}$.

IV. SIMULATION RESULTS

A. Sensitivity Analysis

The global minimum shown in Table II must be verified to consider our model uncertainty. To begin with, an uncertainty of 5% has been considered for the Young's modulus as in [10] while a second moment of area uncertainty of 9% is considered. This last number comes from the way I_{zz} is computed (Eq. 9) with a high influence from the cross-section height. Knowing our manufacturing process, experimental measurements show an uncertainty of 3% (Dektak 150 profilometer) for the manufacturing of the chambers height. For each iteration of the sensitivity analysis, a new optimal tendon tension T^* is computed with the above objective function Ψ (Eq. 13).

This sensitivity analysis, considering the material characteristics and robot manufacturing uncertainties, shows a mean error of the difference between the robot neutral axis and the scala tympani centerline of $\bar{\Psi} = 391.77$ μm and a standard-deviation of $\sigma = 32.4$ μm.

B. Insertion Results

Using the optimal bending stiffness generated previously an insertion profile has been computed from no insertion at $k = N$ or 0% to total-insertion at $k = 0$ or 100%. To proceed so, the objective function Eq. 13 has been modified to consider only the RMSE of the robot beam elements inserted inside the cochlea instead of all the beam elements as depicted in Fig. 6. The optimizer degrees of freedom have also been changed to consider the robot an optimal proximal position $X \in R^3$, the tendon tension T and the rotation

$\mathbf{R}_z(\theta)$ around the normal vector $\vec{e}_z$ the cochlea XY plan to be solved for each k in $[N-1, 0]$:

$$\min_{X, \theta, T} \Psi = \sqrt{\frac{\sum_{i=k}^{N} ||\mathcal{P}(s^*) - \mathcal{M}(i)||^2}{N - k}}$$

subject to : $s^* = \underset{s \in [s_{min}, s_{max}]}{\arg\min} ||\mathcal{P}(s) - \mathcal{M}(i)||$ (14)

as previously explained for Eq. 13. X the robot optimal proximal pose, θ the robot rotation, T the tendon tension and $k \in [0, N]$ the quantity of beam elements outside the cochlea.

In Fig. 6, the robot is in inserted into the cochlea by the means of a sheath as in [18] so that the robot outside the cochlea is constrained and cannot bend. It is possible to follow the scala tympani centerline with the generated design which permit to stay at distance of the anatomy walls and minimize contact.

One should notice that the result in Fig. 6 at $k = 0$ has a better objective function value than in Sec. III. This is explained by the optimization process where $\mathbf{R}_z(\theta)$ was considered constant during the optimal bending stiffness optimization step which is not true anymore during the insertion.

The tendon tension profile depicted in Fig. 7 is crucial for future experiments as each insertion step can be associated with an optimal proximal position X of the robot within its sheath that will be held by a future robot end effector.

These simulation results should be supported by a complete experimental insertion. Until now, only shape and dis-
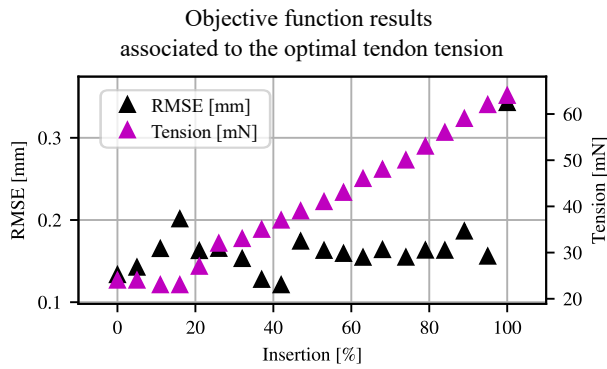
Fig. 7. Evolution of the actuation tendon tension and the RMSE between the robot neutral axis and the Scala Tympani (ST) centerline
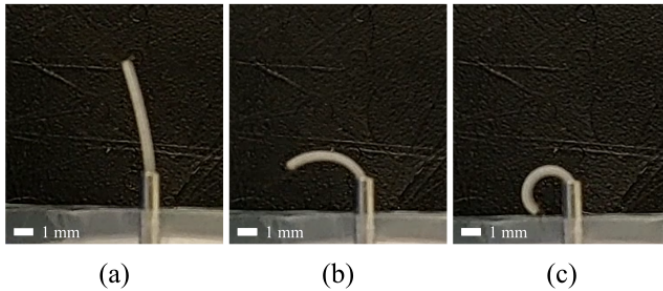

Fig. 8. Current advance for the manufacturing process with a trivial actuated robot.

tance have been considered but in the future experimentation, the only two quality indicators of a good insertion will be: the measured forces against the cochlea with a force sensor and a visual feedback as in [19] to assure that the cochlea is correctly positioned within the scala tymmpani. Current advance in the experimental validation are depicted in Fig. 8 with a tendon actuated cochlear implant at three different actuation force for a given insertion state.

V. CONCLUSION

This paper presented a soft micro-robot optimal design based on optimal bending stiffness in the context of cochlea implant insertion. Here, the implant has been intrinsically actuated with a tendon routed within the implant bulk transforming it into a soft micro-robot capable of changing its own shape based on different tendon tension. A static model using finite-element-method and forward recursion has been employed to obtain the optimal the forward kinematic, the bending stiffness and the optimal insertion path for the generated design. Future work should address the closed-loop insertion and the cochlea implant holder manipulation.

REFERENCES

[1] M Peppi, A Marie, C Belline, J T Borenstein, A Marie, C Belline, and J T Borenstein Intracochlear. Expert Opinion on Drug Delivery Intracochlear drug delivery systems : a novel approach whose time has come. *Expert Opin. Drug Deliv.*, 15(4):319–324, 2018.
[2] Gregory J. Basura, Oliver F. Adunka, and Craig A. Buchman. Scala tympani cochleostomy for cochlear implantation. *Oper. Tech. Otolaryngol. - Head Neck Surg.*, 21(4):218–222, 2010.
[3] Daniele De Seta, Renato Torres, Francesca Yoshie Russo, Evelyne Ferrary, Guillaume Kazmitcheff, Dominique Heymann, Jerome Amiaud, Olivier Sterkers, Daniele Bernardeschi, and Yann Nguyen. Damage to inner ear structure during cochlear implantation: Correlation between insertion force and radio-histological findings in temporal bone specimens. *Hear. Res.*, 344:90–97, 2017.
[4] "About Cochlear Implants" Children's Hospital & Medical Center. *Accessed: Oct. 31, 2023. [Online]. Available: https://www.childrensomaha.org/department/ear-nose-throat/cochlear-implant-program/about-cochlear-implants/*, 2023.
[5] J. R. Clark, L. Leon, F. M. Warren, and J. J. Abbott. Investigation of magnetic guidance of cochlear implants. pages 1321–1326, dec 2011.
[6] Cameron M. Hendricks, Matt S. Cavilla, David E. Usevitch, Trevor L. Bruns, Katherine E. Riojas, Lisandro Leon, Robert J. Webster, Frank M. Warren, and Jake J. Abbott. Magnetic Steering of Robotically Inserted Lateral-wall Cochlear-implant Electrode Arrays Reduces Forces on the Basilar Membrane In Vitro. *Otol. Neurotol.*, 42(7):1022–1030, 2021.
[7] Josephine Granna, Thomas S. Rau, Thien-Dang Nguyen, Thomas Lenarz, Omid Majdani, and Jessica Burgner-Kahrs. Toward automated cochlear implant insertion using tubular manipulators. *Med. Imaging 2016 Image-Guided Proced. Robot. Interv. Model.*, 9786(March 2016):97861F, 2016.
[8] Lena Zentner, Stefan Griebel, and Silke Hügl. Fluid-mechanical compliant actuator for the insertion of a cochlear implant electrode carrier. *Mech. Mach. Theory*, 142:103590, 2019.
[9] Benjamin Arcand, Sudeep Shyamsunder, and Craig Friedrich. A fluid actuator for thin-film electrodes. *J. Med. Devices, Trans. ASME*, 1(1):70–78, 2007.
[10] Jian Zhang and Nabil Simaan. Design of Underactuated Steerable Electrode Arrays for Optimal Insertions. *J. Mech. Robot.*, 5(1):1–11, 2013.
[11] Younan Xia and George M Whitesides. Soft Lithography. *Angew. Chem. Int. Ed.*, 37:550–575, 1998.
[12] Alexandre Thuillier, Sébastien Krut, Nabil Zemiti, and Philippe Poignet. Design optimization of a soft micro-robot for medical intervention. *Accepted. - IEEE Int. Conf. on Advanced Robotics*, 2023.
[13] Helge Rask-andersen and Elsa Erixon. Human Cochlea : Anatomical Characteristics and Their Relevance for Cochlear Implantation. (March 2016), 2011.
[14] B Escude, Clinique Pasteur, and Olivier Deguine. The Size of the Cochlea and Predictions of Insertion Depth Angles for Cochlear. (October), 2006.
[15] Frank Risi. Considerations and rationale for cochlear implant electrode design-past, present and future. *J. Int. Adv. Otol.*, 14(3):382–391, 2018.
[16] Eric Boyer, Alexandre Karkas, Arnaud Attye, Virginie Lefournier, Bernard Escude, and Sebastien Schmerber. Scalar localization by cone-beamcomputed tomography of cochlear implant carriers: A comparative study between straight and periomodiolar precurved electrode arrays. *Otol. Neurotol.*, 36(3):422–429, 2015.
[17] Ronaldo Ariati, Flaminio Sales, Andrews Souza, and Rui A Lima. Polydimethylsiloxane Composites Characterization and Its Applications : A Review. pages 1–21, 2021.
[18] Robert J.S. Briggs, Michael Tykocinski, Roland Lazsig, Antje Aschendorff, Thomas Lenarz, Timo Stöver, Bernard Fraysse, Mathieu Marx, Jr Thomas Roland, Peter S. Roland, Charles G. Wright, Bruce J. Gantz, James F. Patrick, and Frank Risi. Development and evaluation of the modiolar research array - multi-centre collaborative study in human temporal bones. *Cochlear Implants Int.*, 12(3):129–139, 2011.
[19] Daniel Bautista-salinas, Conor Kirby, Mohamed E M K Abdelaziz, Burak Temelkuran, Charlie T Huins, and Ferdinando Rodriguez. Semi-autonomous robotic control of a self-shaping cochlear implant. *2023 IEEE Int. Conf. Robot. Autom.*, (Icra):6823–6829, 2023.